**ORIGINAL ARTICLE**

# The effect of increasing rarefaction on the formation of Edney shock interaction patterns: type-I to type-VI

**M. B. Agir[1]** · **C. White[1]** · **K. Kontis[1]**

## Abstract

A shock–shock interaction problem can arise in high-speed vehicles where an oblique shock from one part of the body impinges on a bow shock from a different part of the body. The nature of the interaction can change as the vehicle increases in altitude to a more rarefied environment. In this work, the outcomes of a numerical study investigating the formation of Edney shock patterns from type-I to type-VI as a result of shock–shock interactions at different rarefaction levels are presented. The computations are conducted with a direct simulation Monte Carlo solver for a free-stream flow at a Mach number of 10. In shock–shock interaction problems, both geometrical and rarefaction parameters determine what type of Edney pattern is formed. The region on the shock impinged surface that experiences enhanced thermo-mechanical loads increases when the free-stream flow becomes more rarefied, but the peak values decrease. It is known that these shock interactions can have unsteady behavior in the continuum regime; the current work shows that although increasing rarefaction tends to move the flow toward steady behavior, under some conditions the flow remains unsteady.

**Graphical abstract**
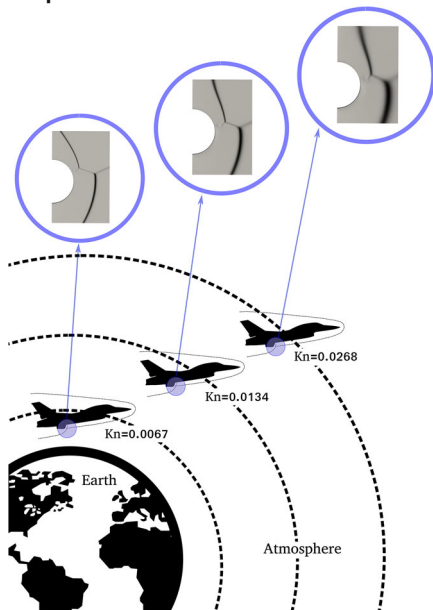


**Keywords** Edney shock–shock interactions · Rarefaction · DSMC · dsmcFoam+ · Hypersonic flow

---

Communicated by S. O'Byrne.

✉ M. B. Agir
m.agir.1@research.gla.ac.uk

C. White
craig.white.2@glasgow.ac.uk

K. Kontis
kostas.kontis@glasgow.ac.uk

[1] Aerospace Sciences, University of Glasgow,
James Watt South Building, Glasgow G12 8QQ, UK

# 1 Introduction

The understanding of shock–shock interaction problems in the aerospace industry has been extensively studied due to their crucial impact on aerodynamic performance and aero-heating characteristics in supersonic and hypersonic flight platforms. A shock–shock interaction problem can arise in high-speed vehicles where an oblique shock from one part on the body impinges on a bow shock from a different part of the body. The result can be greatly increased local pressure and heat loads on a surface [1]. A well-documented example of the problem was detected during an X-15 research flight. An investigation indicated that a shock interaction pattern formed in the vicinity of a ramjet-pylon [2] and severe structural damage was caused by an increase in local heat flux due to an oblique shock generated by the ram jet spike tip, spike flare, or cowl lip interacting with a bow shock ahead of the pylon leading edge.

The shock–shock impingement phenomenon was widely investigated by Edney for different geometries in the blow-down tunnel of Flygtekniska Försöksanstalten (FFA) of Sweden [3,4]. Edney categorized this shock interaction phenomenon with six different types, I–VI, for various regions with respect to where the interaction occurs around a bluff body that is used to create a bow shock. A type-I interaction is formed, and this transitions through types II–VI as the shock interaction point increases in height relative to the body, e.g., a type-VI interaction is formed when the two shocks meet above the solid body. Type-I and type-II exist as a result of the intersection of two shocks from opposite families and these weak interactions create aerothermal loadings because of the crossing of a terminating shock and a boundary layer below the sonic region. The type-III pattern is another weak impingement that creates a shear layer, which is emitted from the shock intersection point and attaches to the bluff body surface. Shock–shock interactions in the vicinity of the stagnation point of a bluff body dramatically increase the heat and pressure loads; the flow exhibits the highest perturbation in type-IV interactions. In this case, the interaction is such that a supersonic jet forms at the first triple point and reaches behind the bow shock, where the flow would otherwise be subsonic. In addition, a shear layer and a transmitted impingement occur at the second triple point. This supersonic jet impingement in type-IV interactions leads to augmented pressure and heat loads where the supersonic jet penetrates behind the bow shock and terminates at the solid surface. As the intersection point moves toward the upper side of the sonic line, the Edney pattern transitions to a type-V interaction, and the effect of the supersonic jet impingement on the surface gradually decreases, but boundary layer interactions still lead to perturbations in heat and pressure loads. In a type-VI pattern, two weak shocks interact and create a supersonic expansion fan, which interacts with the boundary layer. This pattern does not impact local heating and pressure to the same extent as type-IV or type-V interactions; however, type-VI problems are significant in terms of predicting the onset of type-V [5,6].

Sanderson [7] stated that the existence of shock impingement patterns depends on the gas properties, the angle and strength of the shocks, the geometry of the shock generators, and the relative location of impingement on the bow shock. Numerous computational modeling studies have been conducted on shock–shock interactions at hypersonic speeds using continuum approaches [5,8–11]. Furthermore, Kitamura [12] investigated hypersonic heating issues through flux functions, limiters, and reconstructed variables in order to study the shock anomalous and shock-interaction-driven heating. In addition to the CFD solutions, Peng et al. [13] also studied the transitions between type-IVa, type-IV, and type-III shock–shock interaction patterns using a machine learning method. Furthermore, hypersonic flow around a micro-cylinder is modeled with a hybrid rarefied and Navier–Stokes solution [14]. Experimentally, the Edney-type shock–shock interactions were also investigated by Cardona et al. [15] for space debris fragmentation events while the particles re-entry the atmosphere at the speed of Mach 4. In another experiment [16], different sizes of spheres were employed to observe the interactions of bow shocks in a shock tunnel that can be operated at Mach 6. For the design of hypersonic test facilities, CFD and DSMC-based simulations were performed to investigate shock interaction and aerodynamic heating created by a double wedge by the seven organizations [17].

The operation of hypersonic vehicles is likely to take place at high altitudes where the atmosphere becomes rarefied and so the continuum and local thermodynamic equilibrium assumptions can begin to breakdown, i.e., $q \not\propto \frac{\partial T}{\partial x}$ and $\tau \not\propto \frac{\partial u}{\partial y}$, making the use of the Navier–Stokes–Fourier equations questionable. With increasing cruising altitude of hypersonic platforms, the Knudsen number increases and the Reynolds number decreases as the aircraft operates in a relatively low-density atmosphere [18]. Figure 1 summarizes how the structure of a type-IV interaction alters while the platform is increasing the flight altitude.

The dimensionless number that dictates the degree of flow rarefaction is the Knudsen number, $Kn = \frac{\lambda}{L}$, where $\lambda$ is the mean free path of the gas (the average distance an atom/molecule travels between successive intermolecular collisions) and $L$ is a characteristic length scale of the problem. In addition to increasing Knudsen number, the Reynolds number decreases as the aircraft operates in a relatively low-density atmosphere [18]. For rarefied flows, a solution to the Boltzmann equation must be sought to accurately capture the correct physics and flow phenomena.

The modeling of shock–shock interaction heating on the surface of a cowl lip caused by the impingement of a weak

**Fig. 1** A schematic to indicate how the properties of Edney patterns change during a hypersonic flight with an increasing altitude. The shock–shock interaction demonstrations are produced by the dsmcFoam+ computational code
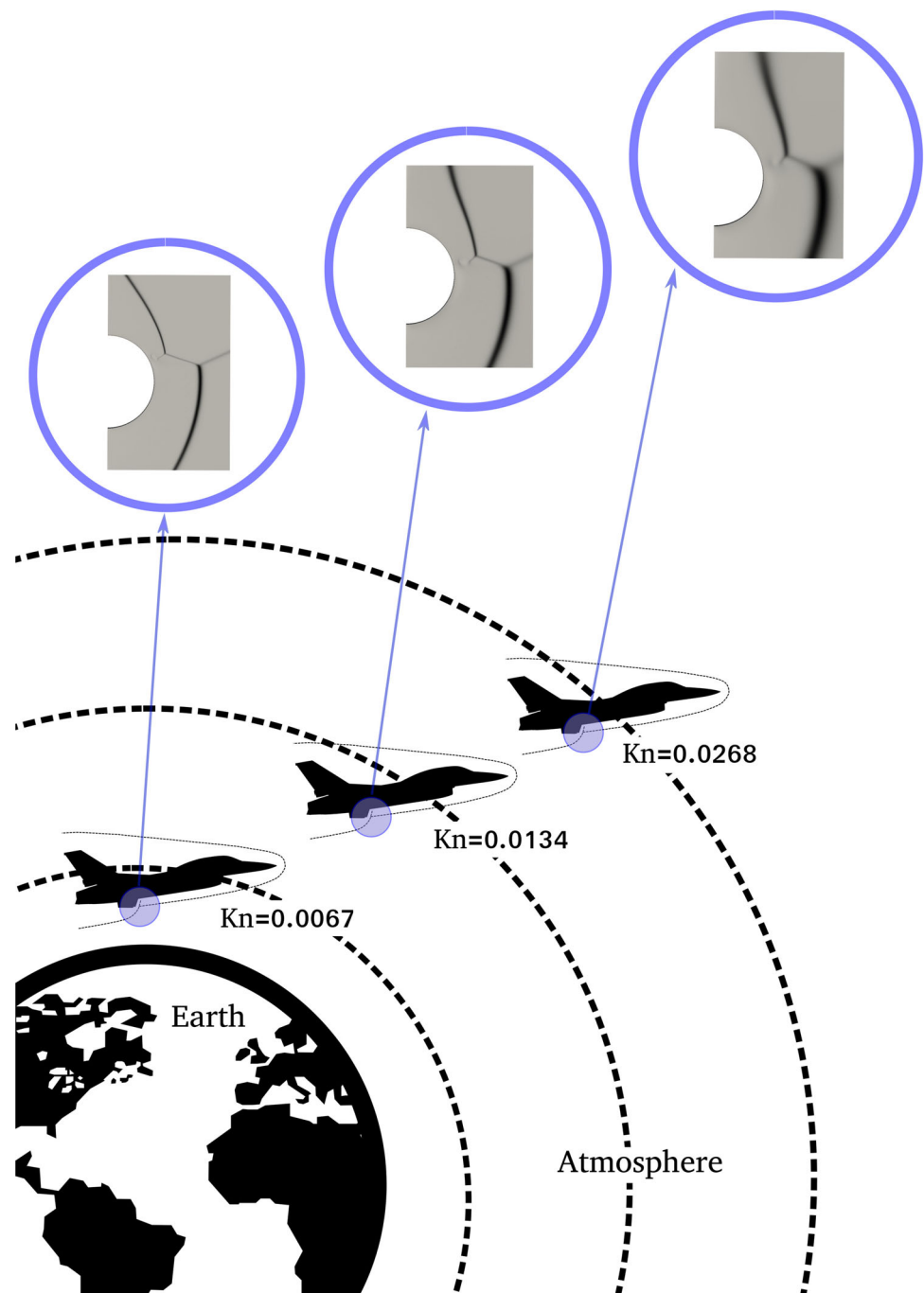
incident shock on a stronger bow shock has been studied in the past. The pioneering study of Pot et al. [19] was conducted via experiment in the French Office National d'Etudes et de Recherches Aérospatiales (ONERA) R5Ch low-density wind tunnel in order to analyze the local heat flux and pressure increase in type-III and type-IV patterns at low Reynolds number. In the experimental setup, a compression ramp forms an oblique shock wave ahead of a strong bow shock generated by the bluff body. The experimental results indicated that a supersonic jet in type-IV and shear layer effects in type-III promoted increased aerothermodynamic loads on the bluff body surface. Although this study provided a dataset for type-III and type-IV Edney shock interactions at a constant rarefaction level, in order to enhance the understanding of the effect of changing flow and geometrical conditions, various geometrical setups with different flow properties are required for a realistic understanding of a hypersonic vehicle with a cruise altitude that takes it through different rarefaction regimes during climb and descent.

Carlson and Wilmoth [20] applied the DSMC method to solve the type-IV interaction for a hypersonic platform at a Mach 15 and 35-km-altitude cruise condition using the two-dimensional/axisymmetric (G2) code of Bird. The authors stated that the flow is in the transition regime as a result of the altitude and that non-continuum and non-equilibrium effects should be taken into account since a purely continuum solution cannot correctly predict the flow physics. In this study, several cases altering the position of the incident shock impingement were performed to distinguish type-IV interactions roughly. The worst-case scenario of type-IV is then selected, with respect to surface heat transfer rather than different geometrical configurations.

Moss et al. [21] simulated the shock–shock and shock and boundary-layer interactions in type-III and type-IV interactions for a generic Mach 10 flight condition, building on the experience of Carlson and Wilmoth [20]. In this study, the ONERA experiment [19] was numerically replicated using the two-dimensional/axisymmetric DSMC code. This study compared the effect of varying distance between the shock generator wedge and the cylinder, which changed the interaction type by altering the impingement location of the incident shock wave. The free-stream properties were kept constant and the surface pressure and heating-rate distributions for eight different shock generator positions were measured. Moss et al. examined only type-III and type-IV interactions at constant Knudsen number.

Xiao et al. [22] conducted a simulation of a double-cone geometry in order to investigate Edney type-IV interactions using various molecular models such as hard sphere, variable hard sphere, and variable soft sphere. The authors presented a comparison of molecular models and experimental results using the pressure coefficient and Stanton number. They found that hard sphere and variable hard sphere models are more accurate than variable soft sphere for the simulations of Edney type-IV shock impingement.

White and Kontis [23] also carried out DSMC simulations to examine the effect of rarefaction on shock interaction physics and surface parameters for a type-IV interaction pattern. The study demonstrated that when the rarefaction level is increased by decreasing gas density, but maintaining all other dimensional parameters the same, the location of the peak in heat transfer, pressure, and skin surface friction coefficients move through the upper sonic line, with the magnitudes of the coefficients decreasing. Mach number contours for three different Knudsen numbers were also compared in the study, which showed the change in impingement location of the incident shock wave and the lack of a supersonic jet and terminating shock as rarefaction increased. Therefore, this study presented a dataset solely for increas-

ing rarefaction; the effect of geometrical configuration was not considered at the same time. The authors employed an open-source DSMC solver implemented within OpenFOAM version 2.4.0, dsmcFoam+ and the solver provides promising results when compared with numerical [21,22] and experimental [19] results in the literature.

Cruise at hypersonic flight produces a complicated flow-field around the aircraft, such as shock–shock interactions. The steadiness of the interaction pattern depends on the geometrical parameters of the shock generators and the flow properties. According to Grasso et al. [24], the impingement location also affects the steadiness of the interaction. Lind and Lewis [25] applied the thin-layer approximation to the two-dimensional Navier–Stokes–Fourier equations to simulate a type-IV case at Mach 8. They observed the formation of unsteadiness, which distorts the flow between the bow shock and shock generator. Shear layers shed between shock layers produced a frequency of unsteadiness, which is associated with the movement of the supersonic jet with the same frequency. Furthermore, the study revealed that the location of peak pressure, the strength of the shock, and the position of shock impingement and supersonic jet flow have a significant impact on the behavior of the flow unsteadiness. Yamamoto et al. [26] focused on the unsteadiness in Edney interactions considering thermochemical non-equilibrium. The authors stated that unsteadiness characteristics are strongly linked to the location of impingement and the standoff distance of the shock. The paper presented detailed information about the period of oscillation and the movement of the supersonic jet, with the unstable behavior being classified as a new type-VII interaction. However, Windisch et al. [27] pointed out that the flow still touches the surface so it can be classified as a type-IVa interaction.

Even when the geometry remains the same, the literature indicates that a change in the degree of rarefaction of the upstream flow leads to different impingement locations and alteration in the strength of the shock waves. Therefore, another significant parameter that can influence the type of Edney shock pattern that is produced is flow rarefaction. In addition, Refs. [7,21] stated the impact of the relative location of the bow shock generator to the oblique shock generator on the flow physics. In the continuum regime, Edney shock interactions can display unsteady [28], but this has not been observed in rarefied flows previously. Therefore, the current work concerns generating a new simulation matrix with varying Knudsen number and shock interaction locations. In the present study, two-dimensional DSMC simulations of eleven different geometries at three different Knudsen numbers are carried out using the dsmcFoam+ code.

## 2 Methodology

### 2.1 Numerical technique

The DSMC method was introduced by Bird in 1963 [29] for probabilistic simulations of dilute gas problems and has become one of the most popular methods for obtaining a solution to the Boltzmann equation in the transition regime. The Boltzmann equation is difficult to solve analytically and expensive to solve numerically. The DSMC method has emerged as one of the most popular techniques for producing a solution to the Boltzmann equation, and it is at its most efficient for high-speed, rarefied flows. DSMC is a transient stochastic particle-based method that uses representative particles in phase space [30,31] to emulate the physics of a real gas. A single DSMC particle represents a large number of real atoms/molecules, reducing the computational expense of the simulation. In DSMC simulations, at least 20 particles per cell are suggested for accurate statistics [32].

In each time step, the particles are moved ballistically according to their current velocity vectors and the time step; any interactions with boundaries are accounted for during this movement phase, which is the first step of the main loop of the DSMC algorithm. The DSMC particles are generated according to a Maxwellian number flux across a boundary interface, usually assuming an equilibrium distribution. Next, particles are indexed according to their current cells to prepare for the collision phase of the algorithm. Collisions are handled in a stochastic manner, with particle velocities being reset and energy exchanged between different modes (translational, rotational, vibrational, electronic) to simulate collision events. Various methods [31,33–36] can be used to ensure that the correct number of collisions take place. In this study, the no-time-counter scheme is applied to select the correct collision rate. This method selects the possible collision pairs in a cell with a volume of $V_{cell}$ from $N$ number of simulated particles. In order for the method to be accurate, the time step must be smaller than the local mean collision time of the gas (so that the movement and collision phases of the algorithm can be decoupled), and the collisions must take place between particles that are located relatively closely together, which is often achieved by only allowing collisions between particles in the same computational cell in the mesh: the cells must also be smaller than local mean free path. The mesh is also used to generate volumes to recover macroscopic properties such as density and temperature from the sampling of particle properties, such as position, thermal velocity, and rotational energy.

DSMC is an unconditionally transient method and so the simulation must be allowed to run until a pseudo-steady condition is reached—if such a condition exists for the flow problem, e.g., some Edney shock interactions exhibit unsteady behavior, as shown in detail later. Once this is reached, the particle properties can be sampled for a long enough period to reduce the scatter in the resolved macroscopic flowfields [32]. The scatter in DSMC results is not a result of the stochastic nature of the method, and it is a natural physical phenomenon that is also present in fully deterministic methods such as molecular dynamics. Unsteady flow features can be captured either through repeating the same simulation many times and producing an ensemble average, or by sampling over relatively small time periods during the transient behavior. The former approach is more accurate, but the latter can provide results to help understand the flow features and mechanisms, with some loss of fidelity.

### 2.2 Computing code

dsmcFoam+ is an open-source solver for dilute gas problems and the greatly extended release[1] of dsmcFoam, which is a DSMC solver within OpenFOAM (or Open-source Field Operation And Manipulation) version 2.4.0 [37–39]. The software is capable of modeling steady and transient flows with many models, including variable hard sphere collisions and the no-time-counter method [37]. A large number of time-steps can be required before the simulation reaches steady state (if one exists for the problem), and then to reduce scatter in the measured macroscopic properties.

### 2.3 High-performance computing

The simulations were carried out on two different high-performance computing clusters at the University of Glasgow. The numerical expense of the DSMC simulations varies according to the rarefaction levels and the level of unsteadiness of shock–shock interactions, which depends on the geometrical setup of the simulated case. In addition, in order to capture the intermolecular collisions more precisely, the meshes are locally refined using an adaptive mesh technique, with refinement regions determined by the sampling of local mean free path data. Although a typical simulation in this work was performed on 24 cores and required 134 h of wall time, the total run time of one simulation varies depending on the number of mesh refinements in order to reach the final result; each case was run multiple times with different locally refined meshes in order to capture the correct intermolecular and surface collisions.

For efficient parallel running, the cases are decomposed such that each core is assigned a similar number of DSMC particles. Approximately one million particles are assigned to each core, but to compensate for the unsteadiness effect, the number of computing cores are increased by 1.3 times in the unsteady simulations. With the movement of the DSMC particles throughout the control volume, the weighting on each

---

[1] https://github.com/MicroNanoFlows/OpenFOAM-2.4.0-MNF.

computational core gradually becomes imbalanced and the performance between the cores changes. The load balancing feature of dsmcFoam+ is used to maintain the distribution of weighting on each core stable by allowing a maximum imbalance of 10% by number density.

## 3 Problem description

In the present work, six types of Edney patterns are investigated by replicating the geometrical dimensions of Refs. [19,21]. The geometry consists of an isosceles triangle shock generator with a 10° leading angle and the wedge was positioned into the flow at an angle of 10° with the horizontal axis. The wedge is represented by a 20° ramp and an extended planar surface with $L_1 = L_2 = 0.50771$ m spanwise length in two-dimensional dsmcFoam+ simulations. The bow shock generator is a cylinder of diameter $D$, with its center located at distance of $L_3$, and a height of $H$. Initially, the longitudinal position of the cylinder center to the leading edge of the wedge and the distance from the horizontal axis are set at $L_3 = 0.102$ m, and $H = 0.053$ m, respectively, as in the reference studies for benchmarking of the dsmcFoam+ results. Afterwards, in order to investigate the variation of shock–shock interaction patterns and augmentation of aerothermodynamic loads on the cylinder surface while the free-stream parameters remain constant, the impingement point of the oblique shock on the bow shock is controlled by altering the $H$ value from 43 to 63 mm in 2-mm increments. The experiment [19] was conducted with a model width-to-cylinder diameter ratio of 6.25. This ratio is assumed to be wide enough that a two-dimensional flow assumption can be made at the center of the length of the cylinder, allowing for two-dimensional dsmcFoam+ simulations to be performed. The schematic of the numerical and experimental setup are illustrated in Fig. 2. In the experiment [19], a contoured nozzle with a diameter of 0.2 m, and a nominal stagnation conditions of 2.5 bar and 1050 K provided a uniform free-stream environment. The test was held with static test conditions of Mach number, $M_\infty = 10$; velocity, $U_\infty = 1450$ m/s; and temperature, $T_\infty = 52.5$ K.

In order to investigate the effect of rarefaction with increasing altitude, the geometrical matrix above is tested at constant Mach number and increasing Knudsen number by reducing the gas density. The relation of the Knudsen, Reynolds, and Mach numbers can be written as $\text{Kn} \propto \frac{M}{\text{Re}}$. The Knudsen number is based on the diameter of the bluff body, $D$, and the mean free path in the free-stream gas, calculated from the variable hard sphere model [40], i.e., $\text{Kn} = \frac{\lambda_\infty}{D}$. The viscosity is calculated from the power law of variable hard sphere for the determination of the Reynolds number, which is $\mu_\infty = 4.99 \times 10^{-6}$ Pa s. The Reynolds number, $\text{Re} = \frac{\rho_\infty U_\infty D}{\mu_\infty}$, is also calculated for each case, and the free-



**Fig. 2** Schematic of the problem setup

**Table 1** Knudsen numbers, Reynolds numbers, and free-stream densities

| Kn | Re | $\rho_\infty$ (kg/m$^3$) |
|---|---|---|
| 0.0067 | 1820 | $3.916 \times 10^{-4}$ |
| 0.0134 | 910 | $1.958 \times 10^{-4}$ |
| 0.0268 | 455 | $9.790 \times 10^{-5}$ |

stream parameters are presented in Table 1 for the different simulations.

For the present study, the non-reacting gas model is considered as a mixture of 21% oxygen and 79% nitrogen, and the energy exchange between the translational, rotational, and vibrational modes is taken into account. The properties of the variable hard sphere model gas species are given in Table 2 in Ref. [23]. The fully diffuse Maxwellian reflection kernel is used to model the gas–surface interactions. The surface temperature is held constant at 300 K. dsmcFoam+ has a varying value of $Z_{\text{vib}}$ that is calculated based on the collision temperature of each individual collision event.

## 4 Results and discussion

In the literature, the Edney shock interaction problem has been studied experimentally and computationally with various DSMC codes from different aspects. This study aims to enlarge that of White and Kontis [23], by extending the geometrical matrix while varying the level of rarefaction. Herein, in order to obtain the effect of increasing rarefaction level on shock–shock interactions, the free-stream flow is considered at three different Knudsen numbers. At the same time, the geometrical setup with altering the vertical position of the bow shock generator cylinder, is $H$, as shown in Fig. 2.

As illustrated in Figs. 3 and 4 in Ref. [23], the pressure and heat transfer coefficients from White and Kontis, calculated using dsmcFoam+, are compared with other studies [19,21,22], which have the same case setup. dsmcFoam+ provides reasonable results when compared with those from

experiment. dsmcFoam+ predicted a peak pressure value of approximately three normalized units greater than experiment, but this difference might be caused by the finite width-to-diameter ratio of the experiment being idealized as two dimensional in the simulations, or a deficiency in the resolution of the pressure tapping holes in the experiment. The dsmcFoam+ outcomes are in a good agreement with other results of numerical references. Furthermore, the heat flux was measured at only ten locations in the experiment, making it difficult to obtain the exact location of the peak value from the experimental data. dsmcFoam+ predicts a maximum heat transfer coefficient of 1.4 on the surface of the bow shock generator cylinder at around $-25°$ (see Fig. 2 and note that negative angles are clockwise in the convention being used), which is in close agreement with the results of experiment and other DSMC codes.

It is highlighted in both numerical references that the size of the numerical mesh is a substantial parameter affecting the accuracy of the results. This is because the mean free path changes locally as the density and temperature gradients form; therefore, local mesh refinement is a necessity to capture the collision statistics correctly. Moss et al. [21] stated that three different meshes were created with 9200 (coarse), 63,510 (intermediate), and 97,060 (fine) cells when the free-stream Knudsen number is constant and indicated the mesh sensitivity using the pressure distributions and surface heating results. In dsmcFoam+, the simulations are run with about one million cells, where local refinement regions are created to ensure the cell sizes are smaller than the local mean free path throughout.

In many practical conditions, these flows are unsteady [41]. Therefore, as the DSMC simulations were being run, the number of DSMC simulators and the average linear kinetic energy were monitored. These properties fluctuate at "steady" state for each case; however, negligibly small changes can be accepted as steady since the unsteady effects, such as shedding of shear layer and movement of the supersonic jet, are not influencing the results. Depending on the rarefaction level and the position of the cylinder, the amplitude of the monitored parameters and their trends can become large, indicating unsteady, cyclical, behavior with time. The flow characteristics of each case, including a statement of whether if was found to have a steady state solution or not, are summarized in Table 2. As seen that the flow conditions are steady for many of the simulations performed (e.g., all values of $H$ greater than 51 mm), but at the two lower Knudsen numbers studied, the flows become unsteady for $H$ of 49 mm and below. An increase in flow rarefaction tends to move the flow back toward a steady solution, as is evident for the results at Kn = 0.0268 at $H$ of 49 mm and below. In addition, an increase in flow rarefaction brings about a change in the Edney interaction type at greater values of $H$, e.g., the interaction remains type-I for $H = 59$ mm and

Kn = 0.0067, but for the same height it becomes a type-II and type-III interaction at Kn = 0.0134 and Kn = 0.0268, respectively.

## 4.1 Steady flowfield

Data presented in this section provide insight to the effects of rarefaction level and varying shock impingement location on the augmentation of aerothermodynamic loading on the cylinder surface and the development of various Edney shock–shock interaction types, as seen in Table 2, when the flow achieves a steady-state solution. Figures 3, 4, 5, 6, 7, 8, 9, 10, and 11 compare the aerothermodynamic properties on the cylinder surface at different Knudsen numbers and values of $H$. Pressure, $C_P$, heat transfer, $C_h$, and surface friction, $C_f$, coefficients are calculated as

$$C_P = \frac{P - P_\infty}{\frac{1}{2}\rho_\infty U_\infty^2} \ (i), \quad C_h = \frac{q}{\frac{1}{2}\rho_\infty U_\infty^3} \ (ii),$$
$$C_f = \frac{\tau}{\frac{1}{2}\rho_\infty U_\infty^2} \ (iii), \tag{1}$$

respectively, where $P$ and $P_\infty$ are local and free-stream pressure, $q$ is local heat flux, $\tau$ is local surface friction, $\rho_\infty$ and $U_\infty$ are the density and velocity of the free-stream.

### 4.1.1 Pressure coefficients

The initial Knudsen number selected is 0.0067, which is the same as previous studies [19,21–23]. Figure 3a shows the distribution of the pressure coefficient on the cylinder surface as $H$ is altered between 63 and 57 mm. At these heights, type-I and type-II patterns are found, with peak pressure coefficients forming between $-10°$ and $-20°$ on the cylinder surface (see Fig. 2); however, the peak moves toward the lower side of the cylinder at $H = 57$ mm, where the flow pattern remains type-II, but is close to becoming a type-III pattern. A strong type-III can then be seen in Fig. 3b at $H = 55$ mm, with a peak at 51.5°. The most severe interactions are at $H = 53$ mm and $H = 51$ mm, which have approximately three times greater pressure coefficient than the type-III interaction. The peak location of pressure shifts from $-30.8°$ at $H = 53$ mm to $-11°$ at $H = 51$ mm. The highest pressure coefficient is found at Kn = 0.0067 when the cylinder center is positioned at $H = 53$ mm. When the distance between the reference surface and the center of the cylinder is decreased below 51 mm, the flowfield structure transforms to unsteady, which is discussed later.
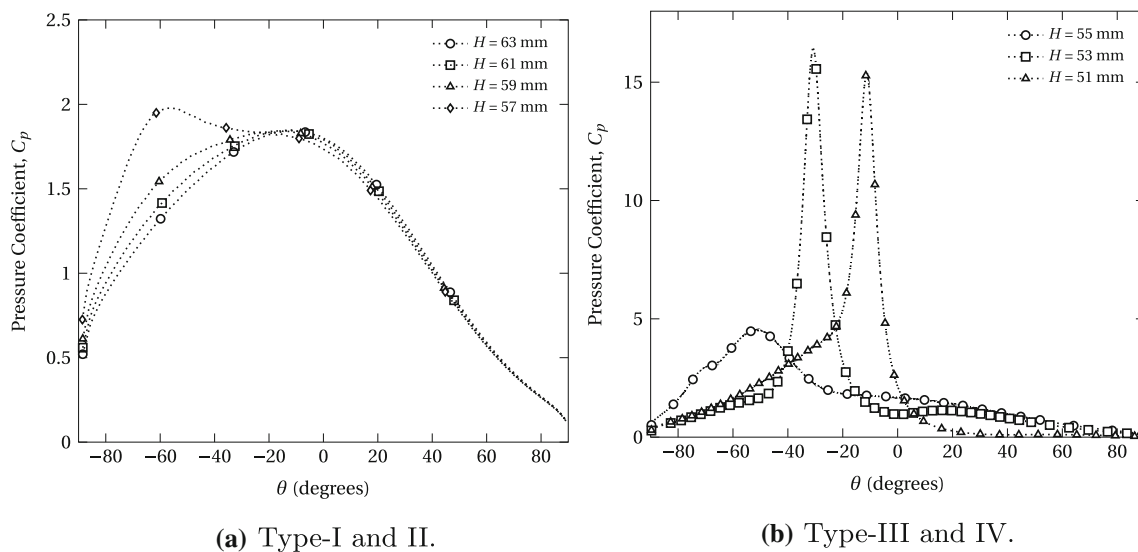
Figure 4 shows the surface pressure coefficients at Kn = 0.0134. The pressure distribution of type-I and type-II interactions shows a similar pattern to those with Kn = 0.0067. In addition, at both Kn = 0.0067 and 0.0134,

**Table 2** The Edney shock interaction types and flow characteristics with changing Knudsen number, and the height at which the center of the cylinder is positioned, $H$

| Kn | $H$ (mm) | | | | | |
|---|---|---|---|---|---|---|
| | 63 | 61 | 59 | 57 | 55 | 53 |
| 0.0067 | Steady | Steady | Steady | Steady | Steady | Steady |
| | Type-I | Type-I | Type-I | Type-II | Type-III | Type-IV |
| 0.0134 | Steady | Steady | Steady | Steady | Steady | Steady |
| | Type-I | Type-I | Type-II | Type-III | Type-IV | Type-IV |
| 0.0268 | Steady | Steady | Steady | Steady | Steady | Steady |
| | Type-I | Type-II | Type-III | Type-IV | Type-IV | Type-IV |

| Kn | $H$ (mm) | | | | |
|---|---|---|---|---|---|
| | 51 | 49 | 47 | 45 | 43 |
| 0.0067 | Steady Type-IV | Unsteady | Unsteady | Unsteady | Unsteady |
| 0.0134 | Steady Type-IV | Unsteady | Unsteady | Unsteady | Unsteady |
| 0.0268 | Steady Type-IV | Steady Type-V | Steady Type-V | Steady Type-VI | Steady Type-VI |



**(a)** Type-I and II.



**(b)** Type-III and IV.

**Fig. 3** Pressure coefficient distributions at Kn = 0.0067

the location of maximum pressure coefficients of type-I interaction patterns is measured as 1.86 at $H = 61$ mm and 63 mm. In terms of type-I interactions, the maximum $C_P$ is found at $-11°$ when Kn = 0.0067 and $H = 61$ mm, and Kn| = 0.0134 and $H = 63$ mm. The stagnation point is located at $-12°$ when Kn = 0.0067 and $H = 63$ mm, and at $-15°$ when Kn = 0.0134 and $H = 61$ mm. As shown in Table 2, a type-II pattern takes place at $H = 59$ mm when Kn = 0.0134; however, a type-II interaction is not found until $H = 57$ mm when Kn = 0.0067. In addition, when the

stagnation point locations are compared for these cases, the peak pressure value can be measured at $-55°$ in both cases but a 1.15 times greater $C_P$ value is found at Kn = 0.0134. Similarly, type-III cases are observed at $H = 57$ mm and $-50°$ when Kn = 0.0134 and at $H = 55$ mm and $\sim -51.5°$ at Kn = 0.0067.

Figure 5 shows the surface pressure coefficients obtained for a flowfield with Kn = 0.0268. The peak value of $C_P$ for a type-I interaction is found at $-50°$, which is further toward the lower side of the cylinder compared with the two lower

**(a)** Type-I and II.

**(b)** Type-III and IV.

**Fig. 4** Pressure coefficient distributions at Kn = 0.0134



**(a)** Type-I, II, III and VI.

**(b)** Type-IV and V.
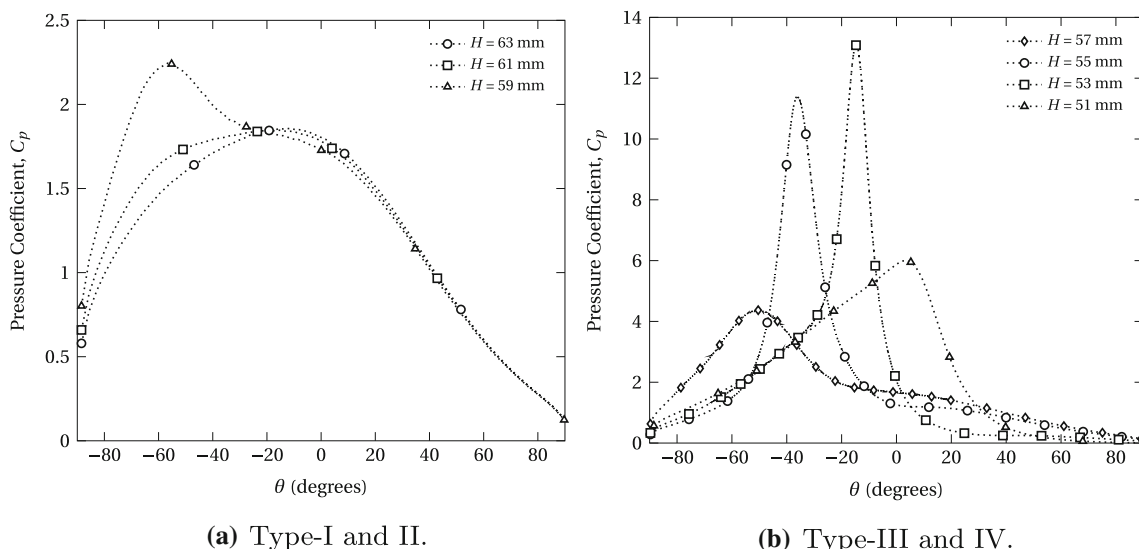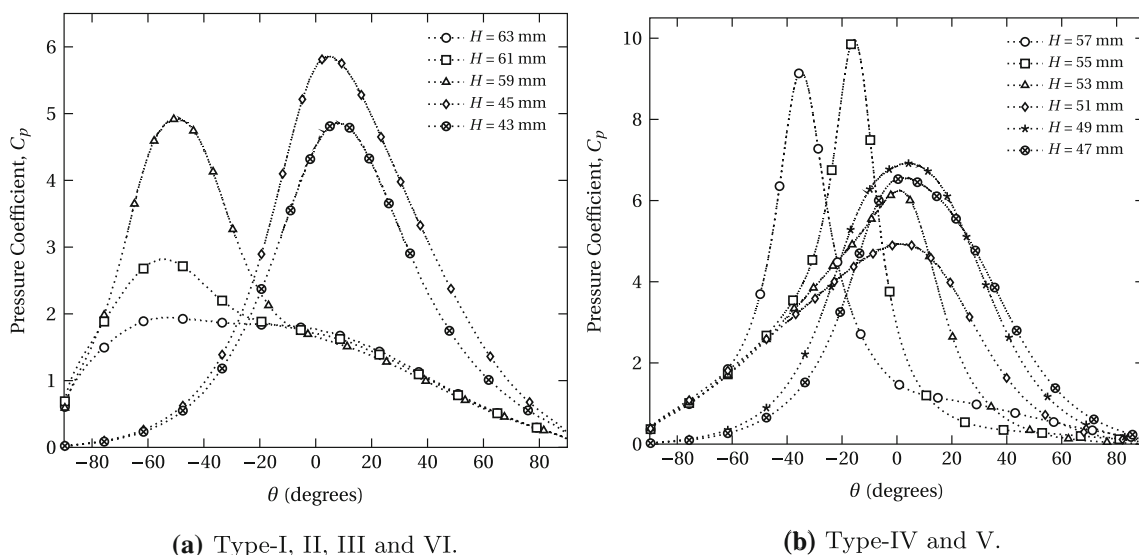
**Fig. 5** Pressure coefficient distributions at Kn = 0.0268

rarefaction levels. In all three Knudsen numbers, the peak locations of the type-II interactions are found at around $-54°$. However, the type-I and type-II patterns have a greater impact on the surface compared with the lower Knudsen numbers and the peak is 1.05 and 1.35 times greater for type-I and type-II interactions, respectively. The maximum impact of type-III interactions for all three Knudsen numbers is found at almost the same location on the surface, $-49°$, with 1.33 times greater magnitude than the averaged value of the lowest and moderate rarefaction levels. At Kn = 0.0067 and 0.0134, type-IV patterns influence the surface pressure coefficients between $-36°$ and $5°$, but the affected zone is slightly restricted at Kn = 0.0268 to $-35°$ to $2°$ at different $H$ values. The transformation of Edney shock types at greater $H$ values

is also found at this rarefaction level. For instance, type-IV is observed for the first time at Kn = 0.0067 and $H = 53$ mm, at Kn = 0.0134 and $H = 55$ mm, and at Kn = 0.0268 and $H = 57$ mm. In addition, the type-IV pattern occupies a wider range of $H$ when the flow becomes more rarefied, i.e., 51–53 mm at Kn = 0.0067, 51–55 mm at Kn = 0.0134, and 51–57 mm at Kn = 0.0268. At $H = 51$ mm and 53 mm for Kn = 0.0268, type-IV patterns become weaker than those for $H = 55$ and 57 mm. Although these two type-IV interactions show the typical pattern of a type-IV impingement with terminating shock near the cylinder surface etc., the type-V cases at $H = 47$ mm and 49 mm have more impact quantitatively on the surface pressure coefficient around $3.25°$. When $H$ is shortened to 43 mm and 45 mm, type-VI interactions

**(a)** Type-I and II.



**(b)** Type-III and IV.

**Fig. 6** Heat transfer coefficient distributions at Kn = 0.0067



**(a)** Type-I and II.



**(b)** Type-III and IV.
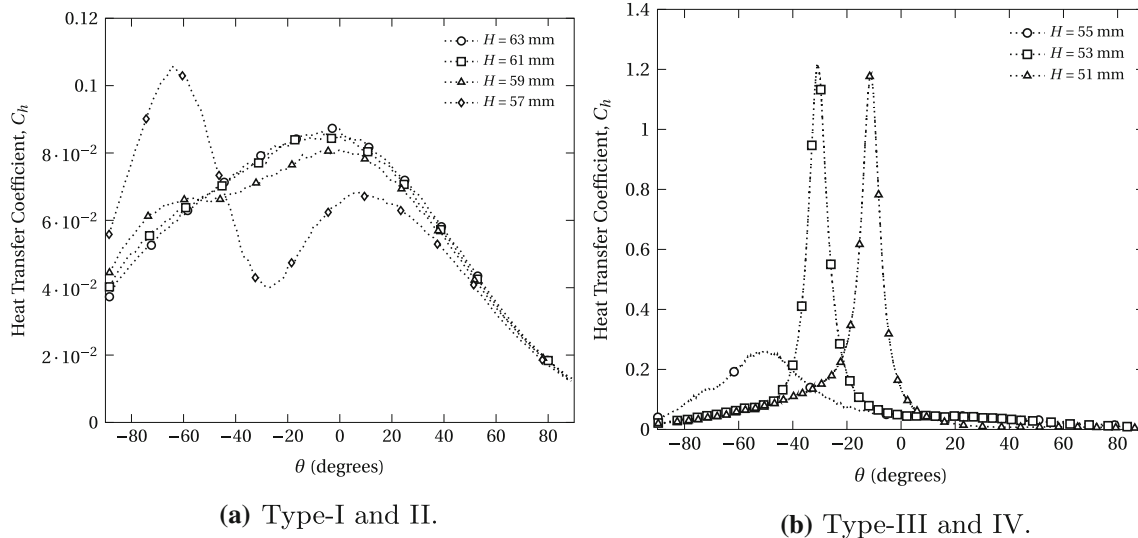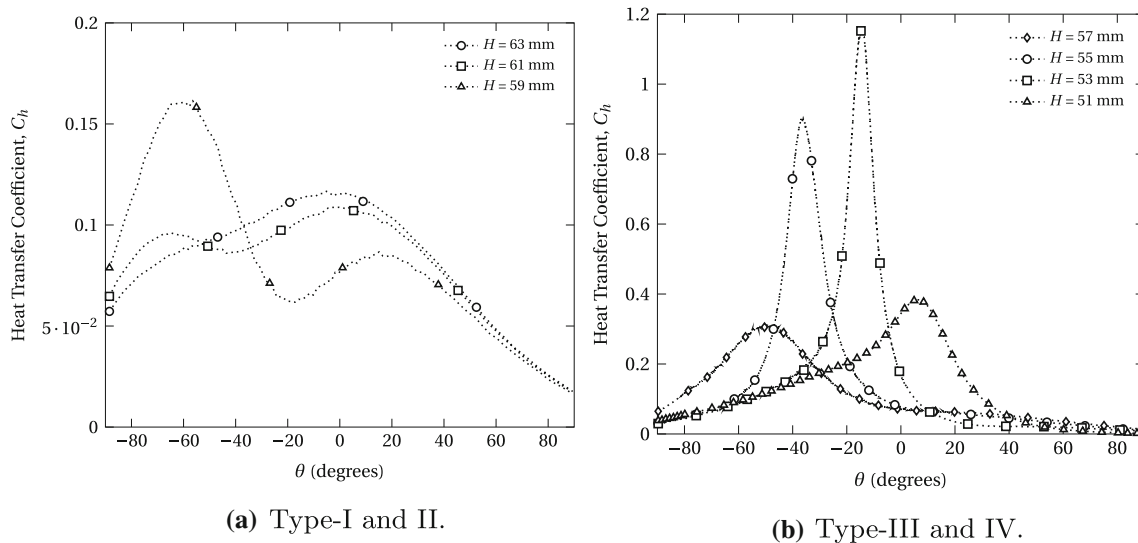
**Fig. 7** Heat transfer coefficient distributions at Kn = 0.0134

are seen in the vicinity of 4.6°–7.3°, with a peak pressure coefficient, which is slightly less than in the type-V interactions.

When the type-IV interactions are compared for all three Knudsen numbers, the interaction produces greater peak pressure coefficients at the less rarefied flowfield condition as shown in Table 3, which is in contrast to the results of the type-I, type-II, and type-III interactions. The highest impact of the type-IV interaction at Kn = 0.0067 and 0.0134 is found at $H = 53$ mm. For Kn = 0.0134 at $H = 51$ mm, the interaction is tending toward a type-V interaction and the peak pressure coefficient is reduced to around 6. At Kn = 0.0268, this evolution of shock patterns starts earlier when $H = 53$ mm as the severity of the type-IV interaction begins decreasing. The maximum pressure coefficient at the

highest Knudsen number is measured at $H = 55$ mm, which is quantitatively the lowest when compared with other the most severe cases both at the lowest and moderate Knudsen numbers.

### 4.1.2 Heat transfer coefficients

Figure 6 shows the augmentation of surface heating coefficient, $C_h$, as a function of vertical separation distance of the cylinder. The results are very similar to the pressure coefficient described above, with the type-I and type-II interactions generating modest increases in the heating load and the type-IV interactions showing severe local heating loads. As expected, the peaks of pressure and heat transfer coef-

**(a)** Type-I, II, III and VI.

**(b)** Type-IV and V.

**Fig. 8** Heat transfer coefficient distributions at Kn = 0.0268



**(a)** Type-I and II.

**(b)** Type-III and IV.
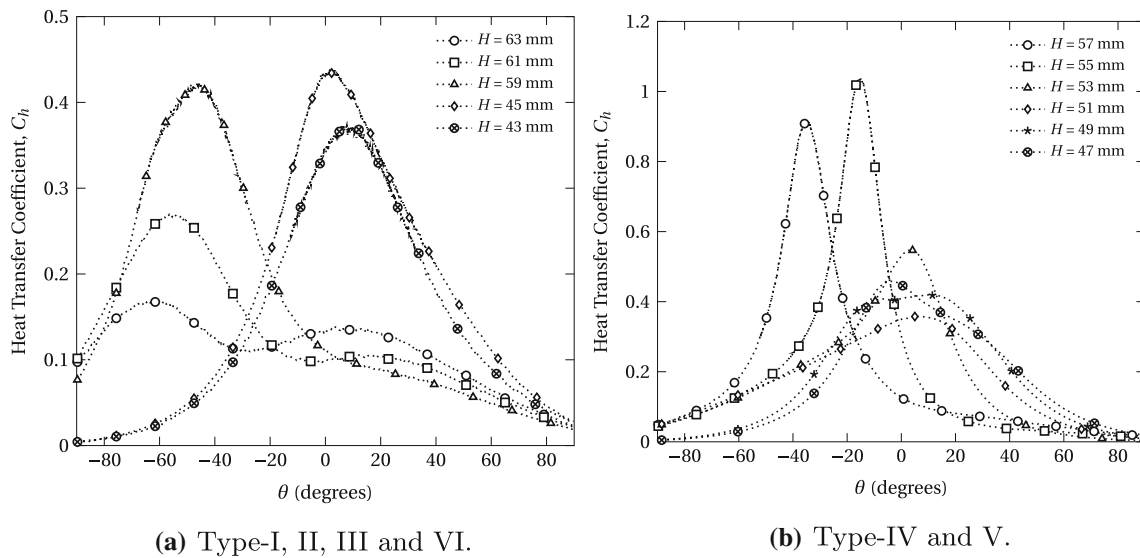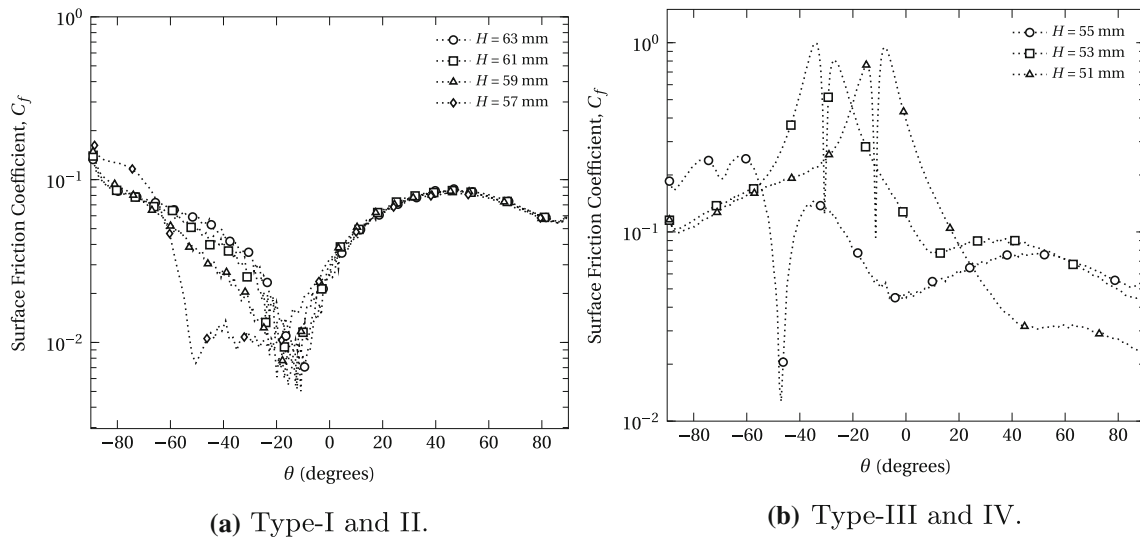
**Fig. 9** Surface friction coefficient distributions at Kn = 0.0067

ficients are located at the same positions on the cylinder surface.

Figures 7 and 8 show the distribution of $C_h$ at Kn = 0.0134 and 0.0268 along the cylinder surface. At first sight, the patterns of surface heating at both the moderate and the highest Knudsen number show similarities to those at Kn = 0.0067; however, it should be emphasized that the impact of the type-I, type-II, and type-III interactions rises with increasing rarefaction. In contrast, the surface heating of the type-IV cases is more severe at Kn = 0.0067 although the number of type-IV patterns increases with increasing rarefaction, which is the same trend as explained in the pressure coefficient section. The aerothermodynamic loads are more evenly distributed along the cylinder surface when the interaction is a type-I or type-II, but is far more localized in the type-IV.

The type-II patterns have a fluctuating trend in Figs. 6a, 7a, and 8a. When the oblique shock impinges at Kn = 0.0067 and $H = 57$ mm, Kn = 0.0134 and $H = 59$ mm, and Kn = 0.0268 and $H = 61$ mm, the maximum surface heating value of the type-II interaction is observed at $-63°$, $-61°$, and $-55°$ on the cylinder surface, respectively. The value of wall heat flux then decreases until $-20°$ at the lowest and the moderate Knudsen number and $0°$ at the highest one; then, at all three Knudsen numbers, a second peak exists, which is quantitatively lesser in magnitude than the first

**(a)** Type-I and II.

**(b)** Type-III and IV.

**Fig. 10** Surface friction coefficient distributions at Kn = 0.0134



**(a)** Type-I, II, III and VI.

**(b)** Type-IV and V.
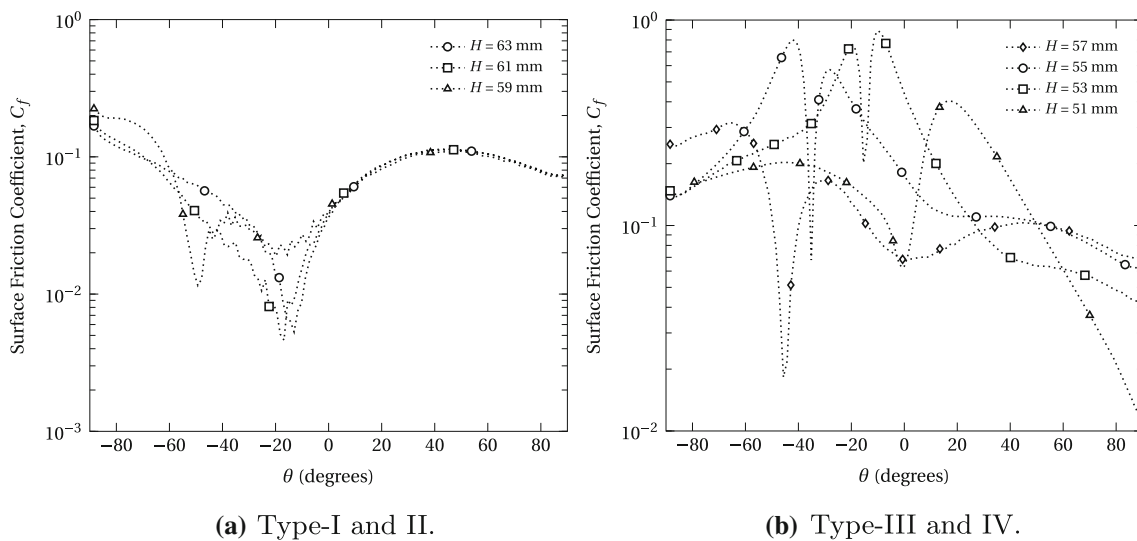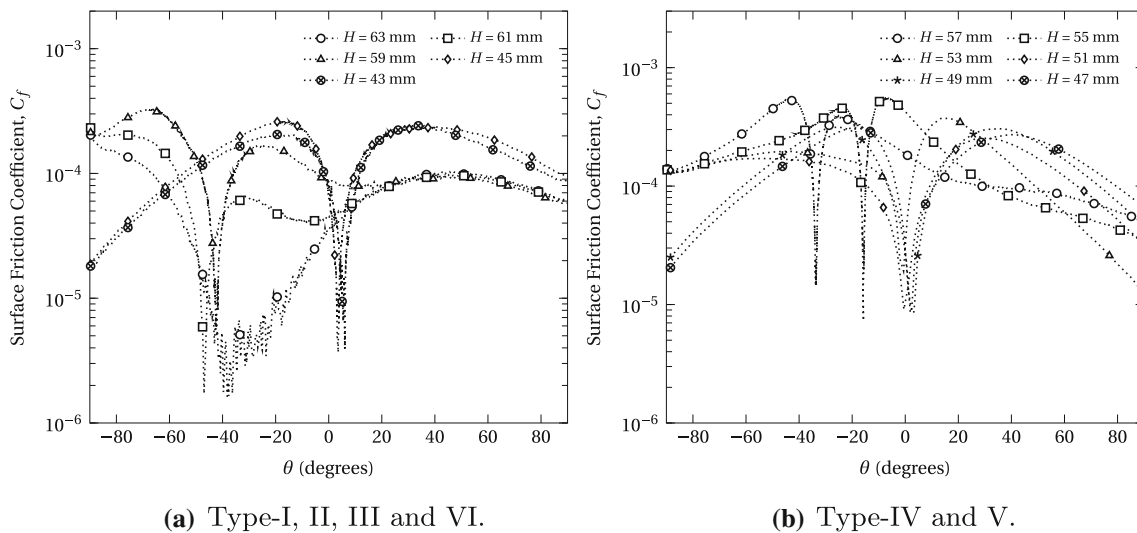
**Fig. 11** Surface friction coefficient distributions at Kn = 0.0268

one. Windisch et al. [27] stated that the surface quantities reflect the flow characteristics. They added, "The closer the jet is located to the wall, the higher the observed wall heat flux." In these cases, the stagnation point exists on the lower side of the cylinder and the section with an upward flow is pushed back from the vicinity of the surface, resulting in a dramatic decrease in heating magnitude, and afterwards the flow begins to reattach to the surface at the location of the second peak.

### 4.1.3 Surface friction coefficients

Figures 9, 10, and 11 show the distributions of the surface friction coefficient. At the stagnation points, there are local minima in the shear stress, with peaks on either side. Again,

the type-III and type-IV interactions show greater peak values of surface friction coefficient than type-I and type-II interactions.

When the surface friction plots are examined, the magnitude of the lowest shear stress is detected around the points of maximum $C_P$ and $C_h$, i.e., at the stagnation point. Compared to the lowest Knudsen number cases, the minimum value of type-I, type-II, and type-III interactions at a moderate Knudsen number (Kn = 0.0134) is slightly greater. However, this situation reverses for type-IV cases where the lowest Knudsen number cases provide greater minimum values. An inspection of Figs. 9b, 10b, and 11b allows for the observation that for type-III and type-IV patterns at the lowest and moderate Knudsen number cases, and type-IV and type-V at the highest Knudsen number cases, the minimum
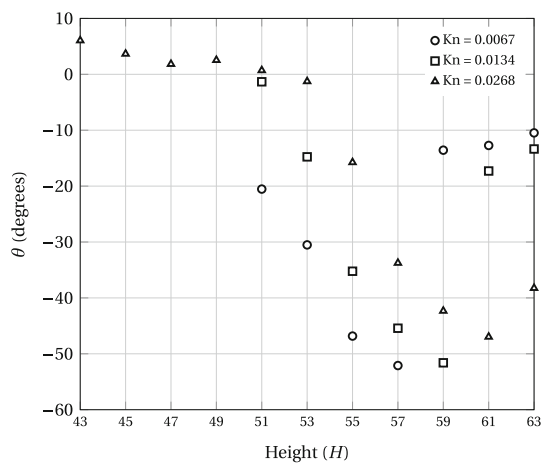
**Fig. 12** The location of $C_f \approx 0$ on the cylinder surface at three different rarefaction levels

surface friction coefficient occurs between two peaks. This flow physics shows that the flow impinges the surface, where the $C_f \approx 0$ and the subsequent flow then begins accelerating across both the upper side and the lower side of the cylinder. The effect of $C_f$ in type-IV and type-V is quite similar, apart from changes in the distribution of friction trends on the surface, and $C_f$ is not as severe at the highest Knudsen number as at the moderate and the lowest ones. The coefficient $C_f$ of type-VI interactions is neither as strong as type-IV and type-V nor as weak as type-I and type-II interactions. The change in location of the peak points of aerothermodynamic loadings on the surface due to alterations in rarefaction levels can also be tracked using $C_f \approx 0$ locations as shown in Fig. 12.

### 4.1.4 Horizontal parameters of flow from the free-stream to the surface

Experimentally, the density and rotational temperature were measured using DL-CARS at ONERA. The parameters were measured at heights of 0 mm to −5 mm along a horizontal line (where 0 mm is the height of the center of the cylinder). In Fig. 13, the dsmcFoam+ results at the $y = -2$ mm location, which is around the height of the first-λ point, are compared with the experimental data. The data collection line crosses different shock interactions depending on rarefaction, i.e., the data collection line is slightly above the first-λ point at Kn = 0.0067; however, the line is positioned just below the second-λ point at Kn = 0.0134 and Kn = 0.0268.

Figure 13a shows the change in normalized density along a line through the shock structures to the cylinder surface. A sudden increase in density can be seen as the bow shock is passed through at a location of $x = -0.007$ m at Kn = 0.0067. As the Knudsen number increases, it is clear that shock stand-off distance increases and the shock wave

becomes more diffuse. The maximum normalized density is measured on the surface and an increase in the normalized density to 20 is obtained at Kn = 0.0134 as the data collection line corresponds to the impingement point of the supersonic jet on the cylinder surface.

Figure 13b, c shows the trends of rotational, $T_r$, and translational, $T_{tr}$ temperatures along the same lines as the density analysis above. The flow temperature increases at $x = -0.007$ m at Kn = 0.0067 as the bow shock is passed through. The flow temperature at the moderate and the higher Knudsen numbers shows an incremental trend as the measurement line is now passing through the complex interaction region as opposed to a bow shock.

### 4.1.5 An overview for the steady flowfield

Surface parameters: The locations of maximum value of $C_h$ and $C_f \approx 0$ on the cylinder surface follow a similar trend to that of $C_P$ as shown in Figs. 5, 8, and 11. In type-I, type-II, and type-III at Kn = 0.0268, the magnitude of $C_h$ is approximately 1.4, 1.625, and 1.35 times, respectively, greater than the measured $C_h$ at Kn = 0.0134. However, $C_f$ at Kn = 0.0268 is lower than the values at the moderate Knudsen numbers. As explained for $C_P$, increasing Knudsen number reduces the aerothermodynamic loading of the type-IV interaction on the surface. For instance, the averaged value of the type-IV patterns at the moderate Knudsen number is 1.38 times greater than those at the highest Knudsen number. In addition to the type-IV cases, stronger interactions occur on the lower side of the surface. Comparing the severity of the type-IV and type-V patterns at Kn = 0.0268 shows that the type-IV interactions, which form around 0° or the upper side of the surface, are slightly weaker than some of type-V interactions. As expected, the effect of the type-VI interactions is slightly weaker than the type-V and stronger than the type-I and type-II patterns. However, shortening $H$ decreases the severity of type-VI interaction gradually and the maximum heating point moves clockwise around the cylinder surface.

In order to compare the effect of changing rarefaction levels, the most severe cases at three different Knudsen numbers are compared in Fig. 14. As previously shown in the data of maximum pressure and heat distributions on the surface, at the lowest and the moderate rarefaction levels, the maximum heat transfer coefficients are at $H = 53$ mm. Figure 14 shows the peak points of surface loading shift clockwise toward 0° with a more significant shift occurring between the lowest and the moderate Knudsen numbers, while there is negligible difference between the moderate and the highest Knudsen numbers. At the highest Knudsen number, the slope of the plot and the magnitude of the heat transfer coefficient are lower than the other two Knudsen numbers; however, unlike the lowest and the moderate Knudsen numbers, the peak value is found at $H = 55$ mm.

**Table 3** Comparison of type-IV cases for all three Knudsen numbers. $H$ is the cylinder height, $\theta$ is the angular position on the cylinder surface where the peak pressure $C_P$ is found
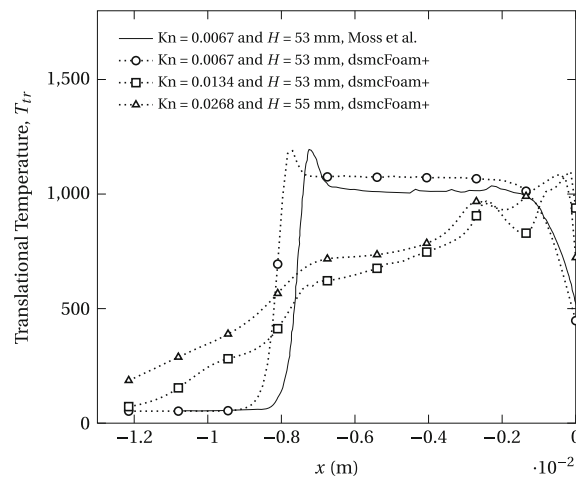
| $H$ (mm) | Kn = 0.0067 | | Kn = 0.0134 | | Kn = 0.0268 | |
|---|---|---|---|---|---|---|
| | $\theta$ | $C_P$ | $\theta$ | $C_P$ | $\theta$ | $C_P$ |
| 57 | | | | | $-35.01$ | 9.18 |
| 55 | | | $-36.14$ | 11.39 | $-15.61$ | 9.96 |
| 53 | $-30.79$ | 16.44 | $-14.41$ | 13.12 | 0.98 | 6.25 |
| 51 | $-11.32$ | 15.32 | 3.86 | 6.02 | 2.11 | 4.94 |
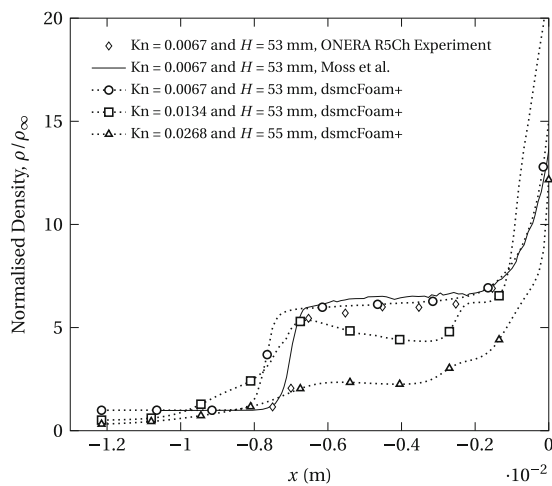


**(a)** Normalised density.
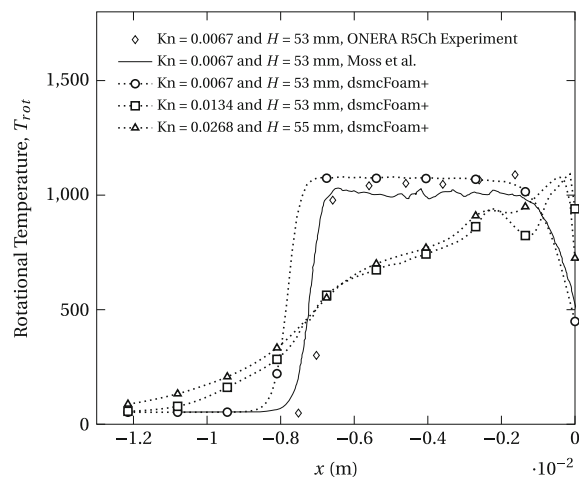


**(b)** Rotational Temperature.



**(c)** Translational Temperature.

**Fig. 13** The comparison of change in density and temperature through free-stream to the surface for the most severe case at each of the three different Knudsen numbers

Flow parameters: When the experimental and numerical results of normalized density are compared, dsmcFoam+ predicts the formation of the bow shock slightly sooner but follows the same trend as the experiment and other numerical work. Furthermore, the outcomes of density and temperature of dsmcFoam+ are consistent. The density increases suddenly as the data collection line passes through the bow shock; however, fluctuations in normalized density depend on rarefaction levels and shock–shock interactions.

For all cases, the data collection line is the same geometrically, but it does not represent the same location of the flow physics, due to the rarefaction effects changing the structure of the flowfield. As seen in Fig. 13, the incident shock intersects the bow shock at Kn = 0.0067 later than other rarefaction levels due to the shorter standoff distance of the bow shock. Therefore, the impingement point is obtained around $x = -8$ mm in both experimental and numerical results for Kn = 0.0067. The post-shock conditions can be examined in the temperature distribution after the peak point. The standoff distance of the bow shock at Kn = 0.0134 and 0.0268 is greater than Kn = 0.0067, which allows for the observation that the increasing trend starting at $x = -12$ mm data extraction line in the Kn = 0.0134 and 0.0268 cases can be explained through a coincidence between the start of the data collection line and the pre-shock region of the oblique shock.

## 4.2 Unsteady flowfield

To address the unsteady mechanisms, the flowfield features are visualized with a synthetic schlieren, and Mach contours at $1.195 \times 10^{-3}$ s for the Kn = 0.0067, $H = 49$ mm case in Fig. 15. The simulations are too large to perform ensemble averaging and so, to reduce the scatter, the results have been averaged for 500 time-steps either side of $1.195 \times 10^{-3}$ s, for a total of 1000 samples. The different unsteadiness phenomena strongly depend on each other, and due to this coupling, the changes in each create impact on others, such as the strength of the shocks, relocation of shocks including the bow shock standoff distance. The impingement of the oblique shock on the bow shock alters the bow shock curvature, which is the first-λ point, and the relocation of the bow shock then causes the formation of the second-λ point below. A supersonic jet forms between the shear layers, which initiates at the λ-points, and following a terminating shock diffuses into the flow behind the bow shock. As the terminating shock diffuses across the upper side of the cylinder, variations can be observed in the bow shock location and curvature, leading to an oscillation in the standoff distance, as indicated by the horizontal green arrow drawn on the bow shock in Fig. 15. The rotation mechanism of the terminating shock is indicated by the white arrows in Fig. 15. In addition, the terminating shock relocates, as indicated in Fig. 17, and contributes to
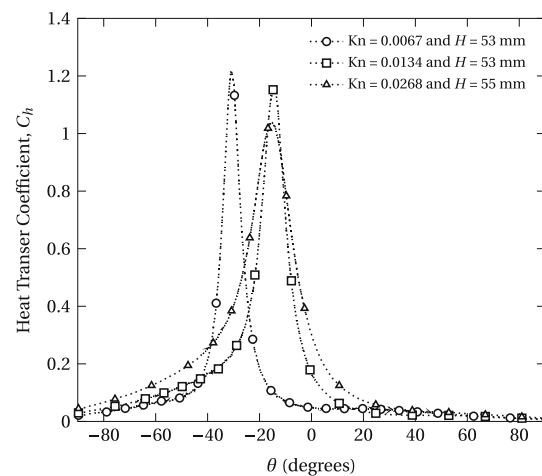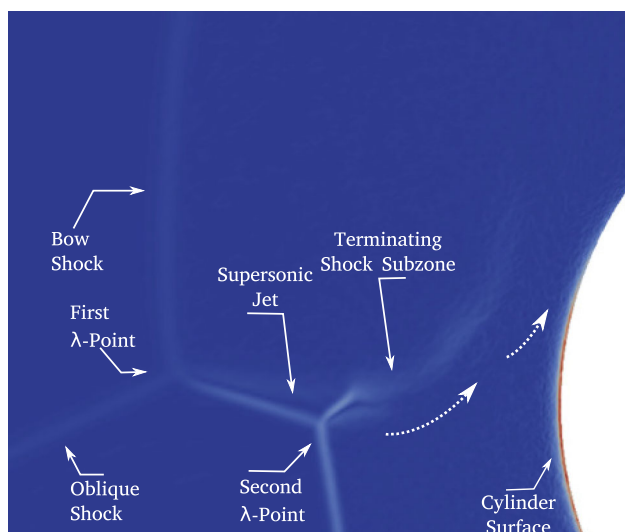


**Fig. 14** The comparison of surface heating by the heat transfer coefficient at the most severe case of three different Knudsen numbers
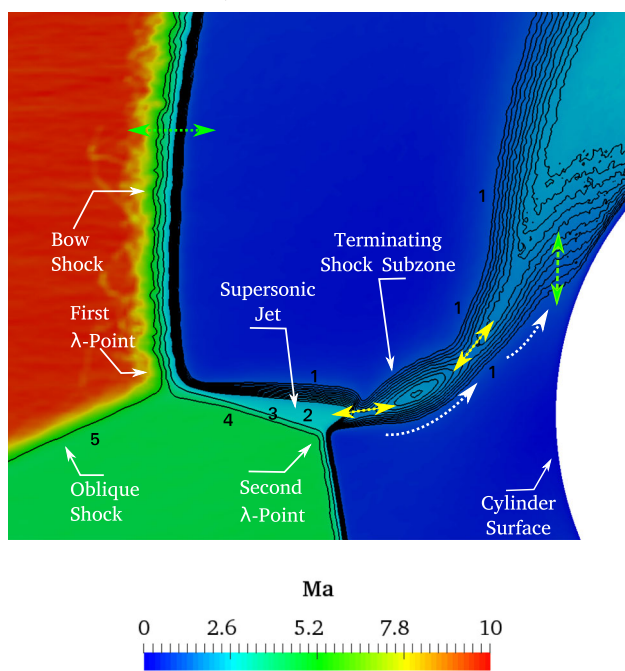
the unsteady mechanism by attaching to (or detaching from) the cylinder surface as shown by the vertical green arrow. The movement through both green arrows are coupled as the shedding effect of the flow has an impact on the standoff distance of the bow shock. The strength of expansion and compression features in the supersonic jet region and the terminating shock subzone vary as they are crucially coupled to the longitudinal compression and expansion of subzones in the direction of yellow arrows. The direct interconnection of a supersonic jet and the terminating shock without interruptions is the usual pattern of a type-IVa shock interaction.

Figure 17 shows the evolution of the flowfield at Kn = 0.0067 and $H = 49$ mm, illustrating the unsteadiness. In this case, the most severe unsteadiness effects are due to the impingement location of the oblique shock. Figure 16 shows that the number of DSMC simulator particles and average linear kinetic energy vary with time and these show oscillations; geometries with a steady-state solution achieve constant values for these properties.

As shown in Fig. 17a, the shock–shock interaction initially takes place at a location horizontally aligned with the center of the cylinder. The experimental result of Grasso et al. [24] showed that the most critical condition happens when the supersonic jet travels nearly perpendicular to the surface as seen in Fig. 17a, which shows the early stage of the impingement and diffusion of the terminating shock in the bow shock. Lind and Lewis [25] stated that the unsteadiness of a type-IV pattern depends on the strength and angle of the oblique shock and the shock impingement location. However, apart from moderate hypersonic flows, the unsteadiness is not related to the changes in hypersonic upstream flow. Ref. [25] expressed the progression of unsteady jet flow as being related to vortices forming at the end of the supersonic jet and eventually being shed along the upper surface of the cylinder. Yamamoto et al. [26] stated that the supersonic jet
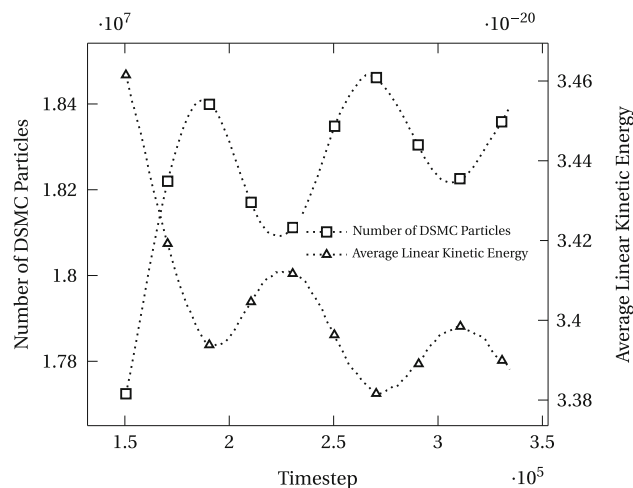
**(a)** Synthetic schlieren



**(b)** Mach Contours

**Fig. 15** Synthetic schlieren and contours of Mach number, showing the unsteady mechanisms in a shock–shock interaction at $H = 49$ mm, Kn = 0.0067, and $t = 1.195 \times 10^{-3}$ s. The numbers on the contour lines denote the Mach numbers



**Fig. 16** Plot showing the number of DSMC particles and average linear kinetic energy in an unsteady simulation; Kn = 0.0134, $H = 49$ mm

different $H$ values at the same rarefaction levels. A notable instance of flow unsteadiness is found at Kn = 0.0067 and $H = 49$ mm, where the type-IVa pattern is relatively stable until $3.3 \times 10^{-3}$ s, but a highly unsteady flow then emerges due to changes in the expansion/compression wave features in the jet flow and deformations in the type-IVa structure are observed between the $3.4 \times 10^{-3}$ s and $3.6 \times 10^{-3}$ s time intervals. An interruption takes place in the terminating shock and the jet flow separates into two parts, where the supersonic flow accelerates through the upper and lower side of the stagnation point and creates a small subsonic region just below the zero degree point of the cylinder surface.

A complete cycle then starts at $\sim 3.6 \times 10^{-3}$ s with the turning of the jet flow along the upper side of the cylinder and ends at $\sim 3.8 \times 10^{-3}$ s, respectively, giving a cycle frequency of $\sim 5$ kHz. At $3.45 \times 10^{-3}$ s, the tip of the terminating shock approaches the cylinder surface, but then starts moving upward together with flow rotation in the terminating shock at $3.6 \times 10^{-3}$ s, which is the approximate start-time of a whole cycle of the jet flow, as shown by the white arrows in Fig. 15. The jet finally reconnects with the upper part of the previously separated jet flow. This transition feature supports the evolution of a type-IV interaction pattern into type-IVa. When reaching the upper turning location at an approximate time of $3.7 \times 10^{-3}$ s and $3.75 \times 10^{-3}$ s, both standoff distance between the near wall and diffused jet flow, and the bow shock to the cylinder significantly decreases. The oscillation of the flowfield completes the half-cycle and begins a downward motion in order to complete the cycle at $3.8 \times 10^{-3}$ s. The driving mechanism of the unsteady movement can be noted as the longitudinal expansion/compression of the supersonic jet and rotations in the terminating shock.
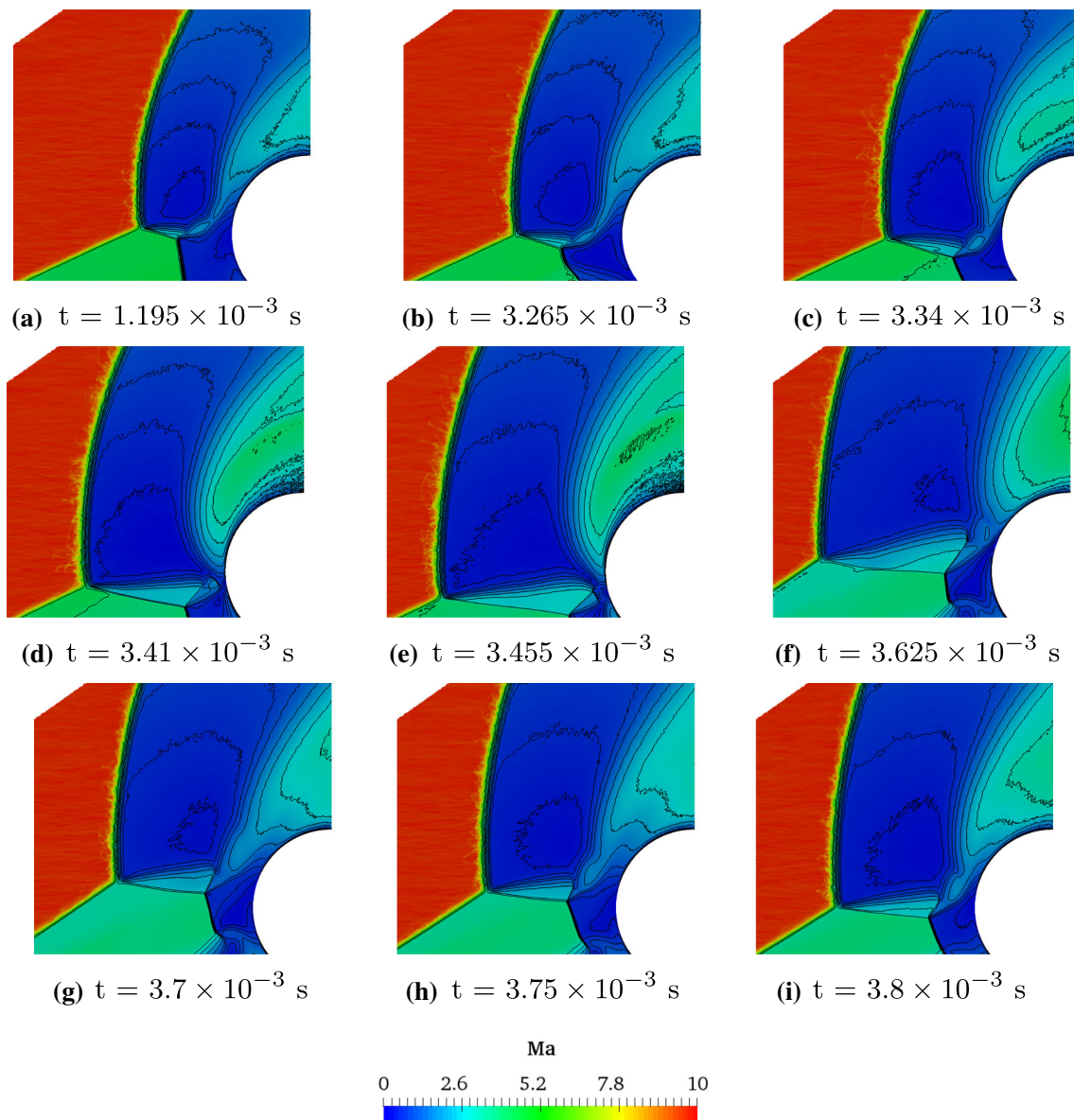
travels toward the upper side of the surface without stagnating. This flow pattern of the supersonic jet detachment lies in the type-IVa classification [27].

The most dominant unsteadiness mechanism in this case is the interconnection of the supersonic jet and the terminating shock as previously mentioned. The flow in the bow shock is neither *inherently stable* nor *periodically unsteady* at the lower and the moderate Knudsen numbers as well as at

**Fig. 17** Mach number contours showing flowfield unsteadiness at Kn = 0.0067, $H = 49$ mm

## 5 Conclusion

Numerical solutions of Edney shock–shock interactions for three different Knudsen numbers and eleven geometrical setups are presented using the DSMC method. Steady flowfields are found for all conducted simulations when $H$ is greater than 51 mm. However, the flows tend to show unsteady behavior at the lowest and the moderate Knudsen numbers for $H$ values of 49 mm or lower. At these heights, the flow reverts back to steady state when the Knudsen number is increased to 0.0268. Computed results of aerothermodynamic loading, such as pressure, surface heating, and friction coefficients on the surface indicate that type-I to type-IV Edney interactions at the lowest and the moderate Knudsen numbers can be observed, but that six types of Edney interactions are captured when the flow reaches the highest Knudsen number. The results show that when the rarefaction level of a non-reacting hypersonic free-stream flow is increased,

1. Type-I, type-II, and type-III cases become more severe,
2. The number of type-IV patterns found increases,
3. When the most severe type-IV cases are sorted in order of strength of shock interactions, greater surface loading occurs at

   – $H = 53$ mm, while the second most severe does so at $H = 51$ mm at the lowest Knudsen number;
   – $H = 53$ mm, and less severe at $H = 55$ mm at the moderate Knudsen number;

– $H = 55$ mm, with the second most severe at $H = 57$ mm.

This shows that the formation of severe type-IV interactions relies on greater $H$ values as the rarefaction level increases.

4. The comparison of maximum heating values at all Knudsen numbers shows that when the flow is more dense, the interaction has the highest impact on the surface and is more focused on a point on the surface. However, going through the more dilute flow, the surface aerothermodynamic loading plots have a more distributed trend and less effect on the surface when compared to lower rarefaction levels,

5. The aerothermodynamic surface loading of the type-IV interactions increases when the pattern tends to change to type-V,

6. Type-VI patterns show a stronger effect than type-I, type-II, type-III at the highest rarefaction level.

Further simulations of shock–shock interactions show that unsteady cases are observed at the lowest and moderate Knudsen numbers at $H = 49$ mm and lower values, where the flow pattern fluctuates between type-IV and type-IVa. In the literature, this effect of supersonic jets, which forms in a region between the upper and the lower shear layers, is discussed to a great extent. However, a tight connection/contribution of the terminating shock effect on the unsteady mechanism and the attachment/detachment of the fringe flow with the movement of pressure waves and the shedding effect are also visibly observed at the lowest Knudsen number when $H = 49$ mm. In addition, the standoff distance of the bow shock oscillates. The rarefaction level has a quantitative impact on the standoff distance. The movement of sub-zones in the post-shock region, e.g., supersonic jet, terminating shock, is strongly coupled and drives the unsteady mechanism. With the increase of rarefaction levels, the energy of the bow shock decreases although the thickness of the bow shock increases.

## References

1. Glass, C.E.: Numerical simulation of low-density shock-wave interactions. Technical Report, NASA/TM-1999-209358 (1999). https://ntrs.nasa.gov/citations/19990063478. Accessed 27th Sept 2022

2. Watts, J.D.: Flight experience with shock impingement and interference heating on the X-15-2 research airplane. Technical Report, NASA/TM-X-1669 (1968). https://www.nasa.gov/centers/dryden/pdf/87756main_H-524.pdf. Accessed 27th Sept 2022

3. Edney, B.E.: Anomalous heat transfer and pressure distributions on blunt bodies at hypersonic speed in the presence of an impinging shock. Technical Report, FFA-115 (1968). https://doi.org/10.2172/4480948

4. Edney, B.E.: Effects of shock impingement on the heat transfer around blunt bodies. AIAA J. **6**(1), 15–21 (1968). https://doi.org/10.2514/3.4435

5. Glass, C.E.: Computer program to solve two-dimensional shock-wave interference problems with an equilibrium chemically reacting air model. Technical Report, NASA/TM-4187 (1990). https://ntrs.nasa.gov/api/citations/19920022003/downloads/19920022003.pdf. Accessed 27th Sept 2022

6. Morris, D.J., Keyes, J.W.: Computer programs for predicting supersonic and hypersonic interference flow fields and heating. Technical Report, NASA/TM-X-2725 (1973). https://ntrs.nasa.gov/citations/19730016558. Accessed 27th Sept 2022

7. Sanderson, S.R., Sturtevant, B.: Shock wave interactions in hypervelocity flow. Proceedings of Shock Waves at Marseille, vol. 1, pp. 69–74 (1995). https://doi.org/10.1007/978-3-642-78829-1_10

8. Garbacz, C., Maier, W.T., Scoggins, J.B., Economon, T.D., Magin, T., Alonso, J.J., Fossati, M.: Shock interactions in inviscid air and $CO_2$–$N_2$ flows in thermochemical non-equilibrium. Shock Waves **31**, 239–253 (2021). https://doi.org/10.1007/s00193-021-00999-8

9. Garbacz, C., Fossati, M., Maier, W., Alonso, J.J., Scoggins, J., Magin, T., Economon, T.D.: Numerical study of shock interference patterns for gas flows with thermal nonequilibrium and finite-rate chemistry. AIAA SCITECH 2020 Forum, Orlando, FL, AIAA Paper 2020-1805 (2020). https://doi.org/10.2514/6.2020-1805

10. Durna, A., Celik, B.: Time-periodic shock interaction mechanisms over double wedges at Mach 7. Shock Waves **29**(3), 381–399 (2019). https://doi.org/10.1007/s00193-018-0864-7

11. Yang, L., Yue, L., Zhang, Q., Zhang, X.: Numerical study on the shock/combustion interaction of oblique detonation waves. Aerosp. Sci. Technol. **104**, 105938 (2020). https://doi.org/10.1016/j.ast.2020.105938

12. Kitamura, K.: Assessment of SLAU2 and other flux functions with slope limiters in hypersonic shock-interaction heating. Comput. Fluids **129**, 134–145 (2016). https://doi.org/10.1016/j.compfluid.2016.02.006

13. Peng, J., Luo, C.T., Han, Z.J., Hu, Z.M., Han, G.L., Jiang, Z.L.: Parameter-correlation study on shock–shock interaction using a machine learning method. Aerosp. Sci. Technol. **107**, 106247 (2020). https://doi.org/10.1016/j.ast.2020.106247

14. Darbandi, M., Roohi, E.: A hybrid DSMC/Navier–Stokes frame to solve mixed rarefied/nonrarefied hypersonic flows over nano-plate

and micro-cylinder. Int. J. Numer. Methods Fluids **72**(9), 937–966 (2013). https://doi.org/10.1002/fld.3769

15. Cardona, V., Joussot, R., Lago, V.: Shock/shock interferences in a supersonic rarefied flow: experimental investigation. Exp. Fluids **62**(6), 1–14 (2021). https://doi.org/10.1007/s00348-021-03225-4
16. Park, S.-H., Park, G.: Separation process of multi-spheres in hypersonic flow. Adv. Space Res. **65**(1), 392–406 (2020). https://doi.org/10.1016/j.asr.2019.10.009
17. Knight, D., Chazot, O., Austin, J., Badr, M.A., Candler, G., Celik, B., de Rosa, D., Donelli, R., Komives, J., Lani, A., Levin, D., Nompelis, I., Panesi, M., Pezzella, G., Reimann, B., Tumuklu, O., Yuceil, K.: Assessment of predictive capabilities for aerodynamic heating in hypersonic flow. Prog. Aerosp. Sci. **90**, 39–53 (2017). https://doi.org/10.1016/j.paerosci.2017.02.001
18. Cheng, H.: Perspectives on hypersonic viscous flow research. Annu. Rev. Fluid Mech. **25**(1), 455–484 (1993). https://doi.org/10.1146/annurev.fl.25.010193.002323
19. Pot, T., Chanetz, B., Lefebvre, M., Bouchardy, P.: Fundamental study of shock/shock interference in low density flow. 21st International Symposium on Rarefied Gas Dynamics, Marseille, France, Paper 1998-40 (1998)
20. Carlson, A.B., Wilmoth, R.G.: Shock interference prediction using direct simulation Monte Carlo. J. Spacecr. Rockets **29**(6), 780–785 (1992). https://doi.org/10.2514/3.25531
21. Moss, J.N., Pot, T., Chanetz, B., Lefebvre, M.: DSMC simulation of shock–shock interactions: emphasis on type IV interactions. Technical Report, Document ID: 20040086965 (1999). https://ntrs.nasa.gov/citations/20040086965. Accessed 27th Sept 2022
22. Xiao, H., Shang, Y., Wu, D.: DSMC simulation and experimental validation of shock interaction in hypersonic low density flow. Sci. World J. **2014**, 732765 (2014). https://doi.org/10.1155/2014/732765
23. White, C., Kontis, K.: The effect of increasing rarefaction on the Edney type IV shock interaction problem. Proceedings of the 22nd International Shock Interactions Symposium, Glasgow, UK, July 4–8, 2016, pp. 299–311 (2018). https://doi.org/10.1007/978-3-319-73180-3_23
24. Grasso, F., Purpura, C., Chanetz, B., Délery, J.: Type III and type IV shock/shock interferences: theoretical and experimental aspects. Aerosp. Sci. Technol. **7**(2), 93–106 (2003). https://doi.org/10.1016/S1270-9638(02)00005-6
25. Lind, C.A., Lewis, M.J.: Computational analysis of the unsteady type IV shock interaction of blunt body flows. J. Propul. Power **12**(1), 127–133 (1996). https://doi.org/10.2514/3.24000
26. Yamamoto, S., Takasu, N., Nagatomo, H.: Numerical investigation of shock/vortex interaction in hypersonic thermochemical nonequilibrium flow. J. Spacecr. Rockets **36**(2), 240–246 (1999). https://doi.org/10.2514/2.3438
27. Windisch, C., Reinartz, B.U., Müller, S.: Investigation of unsteady Edney type IV and VII shock–shock interactions. AIAA J. **54**(6), 1846–1861 (2016). https://doi.org/10.2514/1.J054298
28. Khatta, A., Gopalan, J.: Hypersonic shock tunnel studies of Edney type III and IV shock interactions. Aerosp. Sci. Technol. **72**, 335–352 (2018). https://doi.org/10.1016/j.ast.2017.11.001
29. Bird, G.A.: Breakdown of translational and rotational equilibrium in gaseous expansions. AIAA J. **8**(11), 1998–2003 (1970). https://doi.org/10.2514/3.6037
30. Bird, G.A.: Molecular Gas Dynamics and the Direct Simulation of Gas Flows. Clarendon Press, Oxford, UK (Oxford Engineering Science Series) (1994)
31. Bird, G.A.: The DSMC Method. CreateSpace Independent Publishing Platform (2013)
32. Hadjiconstantinou, N.G., Garcia, A.L., Bazant, M.Z., He, G.: Statistical error in particle simulations of hydrodynamic phenomena. J. Comput. Phys. **187**(1), 274–297 (2003). https://doi.org/10.1016/S0021-9991(03)00099-8
33. Stefanov, S.K.: On DSMC calculations of rarefied gas flows with small number of particles in cells. SIAM J. Sci. Comput. **33**(2), 677–702 (2011). https://doi.org/10.1137/090751864
34. Venkattraman, A., Alexeenko, A.A., Gallis, M.A., Ivanov, M.S.: A comparative study of no-time-counter and majorant collision frequency numerical schemes in DSMC. AIP Conf. Proc. **1501**(1), 489 (2012). https://doi.org/10.1063/1.4769577
35. Goshayeshi, B., Roohi, E., Stefanov, S.: DSMC simulation of hypersonic flows using an improved SBT-TAS technique. J. Comput. Phys. **303**, 28–44 (2015). https://doi.org/10.1016/j.jcp.2015.09.027
36. Taheri, E., Roohi, E., Stefanov, S.: A symmetrized and simplified Bernoulli trial collision scheme in direct simulation Monte Carlo. Phys. Fluids **34**(1), 012010 (2022). https://doi.org/10.1063/5.0076025
37. Scanlon, T.J., Roohi, E., White, C., Darbandi, M., Reese, J.M.: An open source, parallel DSMC code for rarefied gas flows in arbitrary geometries. Comput. Fluids **39**(10), 2078–2089 (2010). https://doi.org/10.1016/j.compfluid.2010.07.014
38. White, C., Borg, M.K., Scanlon, T.J., Reese, J.M.: A DSMC investigation of gas flows in micro-channels with bends. Comput. Fluids **71**, 261–271 (2013). https://doi.org/10.1016/j.compfluid.2012.10.023
39. White, C., Borg, M.K., Scanlon, T.J., Longshaw, S.M., John, B., Emerson, D., Reese, J.M.: dsmcFoam+: an OpenFOAM based direct simulation Monte Carlo solver. Comput. Phys. Commun. **224**, 22–43 (2018). https://doi.org/10.1016/j.cpc.2017.09.030
40. Bird, G.A.: Definition of mean free path for real gases. Phys. Fluids **26**(11), 3222–3223 (1983). https://doi.org/10.1063/1.864095
41. Holden, M.S., Wadhams, T.P.: A review of experimental studies for DSMC and Navier–Stokes code validation in laminar regions of shock/shock and shock boundary layer interaction including real gas effects in hypervelocity flows. 36th AIAA Thermophysics Conference, Orlando, FL, AIAA Paper 2003-3641 (2003). https://doi.org/10.2514/6.2003-3641